Acta Crystallographica Section A
Foundations of Crystallography
ISSN 0108-7673

Received 5 February 2001
Accepted 26 April 2001

Applications of dynamical diffraction under locally plane wave conditions: defects in nearly perfect crystals and X-ray refractometry

V. Mocella,[a,b]* Y. Epelboin,[c] J. P. Guigay[d] and J. Härtwig[d]

[a]User Program Division, Advanced Photon Source, Argonne National Laboratory, IL 60439, USA, [b]INFM – Operative Group in Grenoble, c/o European Synchrotron Radiation Facility, BP 220, 38043 Grenoble CEDEX, France, [c]Laboratoire de Minéralogie–Cristallographie, URA 009 CNRS, Universités P. M. Curie et D. Diderot, Case 115, 75252 Paris CEDEX 05, France, and [d]European Synchrotron Radiation Facility, BP 220, 38043 Grenoble CEDEX, France. Correspondence e-mail: mocella@esrf.fr

In a previous paper, the concept of a locally plane wave was explained theoretically. In such a configuration, the fringe pattern recorded on the film can be considered as a phase analyser. Here the experimental analysis is presented, showing examples of interesting applications to X-ray refractometry and to the visualization of the strain field around isolated defects.

1. Introduction

In previous papers (Mocella *et al.*, 1999, 2000), we have shown that, under specific conditions which are fulfilled at the long beamline ID19 of the ESRF, the incident spherical wave can be considered as a locally plane wave in a Bragg diffraction experiment. This means that each point along the exit surface of the crystal 'sees' a locally plane wave having an angular deviation from the exact Bragg condition depending on the position of this point. We have shown that the intensity profile recorded across the beam diffracted by a perfect crystal, in the Laue geometry, reproduces the oscillations of the rocking curve. These oscillations, which arise from the Pendellösung interferences between the wavefields inside the crystal, are very sensitive to phase perturbations in the propagation of the X-rays. Phase perturbations induce visible changes in the recorded intensity profile. The sensitivity of this profile to the phase of the incident wavefront allows the detection of phase modifications, produced along the path of the incident beam, either outside or inside the crystal. In this paper, we shall present applications of this phenomenon to a quantitative refractive index measurement of the crystal and to the direct visualization of the strain field associated with isolated defects in the crystal.

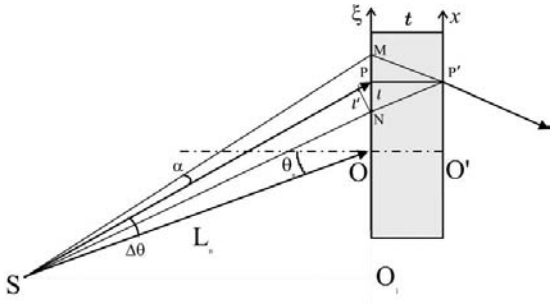

Figure 1
Geometry of the locally plane wave setting. The exact Bragg condition corresponds to point O. In the considered symmetrical case, the coordinate ξ of the point P' is equal to the coordinate x of the point P which is the middle of the influence domain MN on the entrance surface.

2. The locally plane wave conditions

We will first recall the main results explained in detail by Mocella *et al.* (2000). Let us consider a plane parallel crystal plate of thickness t, in a symmetrical Laue geometry (Fig. 1), with Bragg angle θ_B set for the central part of the incident beam. As explained by Mocella *et al.* (2000), one can establish a relation between the local angle of incidence $\theta(\xi)$ and the coordinate ξ of any point, along the entrance surface of the crystal,

$$\Delta\theta_{\rm in}(\xi) = \theta(\xi) - \theta_B = \xi \cos\theta_B/(L_0), \qquad (1)$$

where L_0 is the source-to-crystal distance, $\Delta\theta_{\rm in}(\xi)$ is the departure from the Bragg condition which is exactly satisfied for $\xi = 0$.

The portion of the incident wavefront on the entrance surface contributing to the diffracted wave at a point P' on the exit surface is strictly limited (Authier & Simon, 1968) by the intersection of the entrance surface with the two lines drawn from P' in the incident and in the reflected directions (segment MN in Fig. 1). In this 'influence domain', of half-width $l = t\tan\theta_B$ along the entrance surface, the sphericity of the wavefront can be neglected if the maximum distance between the spherical wavefront and its tangential plane, estimated in the paraxial approximation as $(t\sin\theta_B)^2/2L_0$, is smaller than $\lambda/2$ [equations (9) and (10) in Mocella *et al.* (2000)],

$$l \ll (\lambda L_0)^{1/2}/\cos\theta_B \iff t \ll (\lambda L_0)^{1/2}/\sin\theta_B \equiv t_{lp}. \qquad (2)$$

Condition (2) means that the projection $l' = l\cos\theta_B$ of the influence domain on the plane perpendicular to the incident direction is much smaller than the radius of the Fresnel zone, $(\lambda L_0)^{1/2}$.

Condition (2) is well satisfied in our experiments at the ID19 beamline at the ESRF since $L_0 = 145$ m. We may thus consider that each point of coordinate ξ along the entrance plane 'sees' a *locally plane wave* in off-Bragg position $\Delta\theta_{in}(\xi)$ given by (1). The intensity profile $I(x)$ in the reflected beam reproduces the reflectivity curve $R(\theta - \theta_B)$, also called the 'rocking curve', usually defined as the measured reflectivity when the crystal is rotated around the Bragg position in a parallel incident beam. Consequently, if condition (2) is satisfied, the intensity distribution $I(x)$ of the topograph is $I(x) = R(x \cos\theta_B / L_0)$ and appears as a set of parallel fringes as shown in Fig. 2. These fringes are regularly spaced, except in the central region of the pattern, with a spacing equal to $\lambda L_0 / t \sin(2\theta_B)$ (*e.g.* Pinsker, 1978).

The finite size of the source produces a blurring of the fringe pattern. It is easy to understand, from Fig. 1, that a displacement of the point source S, along the x direction, corresponds to the same displacement of the fringe pattern; therefore, the size a of the source along the x direction must be much smaller than the fringe spacing, in order to preserve the visibility of the fringes. This is expressed as

$$a \ll \lambda L_0 / (t \sin 2\theta_B). \tag{3}$$

The lateral (or spatial) coherence width (Born & Wolf, 1983) perpendicular to the incident direction is defined as $\lambda L_0 / (a \cos\theta_B)$. Condition (3) can therefore be interpreted by saying that the lateral coherence width must be much larger than the full width $2l'$ of the influence domain in the plane perpendicular to the mean incident direction. The width $2l' = 2l \cos\theta_B = 2t \sin\theta_B$ is the projection of the segment MN in this plane (Fig. 1).

The fringe pattern is also blurred by the wavelength bandwidth. A change $\Delta\lambda$ of the wavelength λ induces a change $\Delta\theta_B = \Delta\lambda / \lambda \tan\theta_B$ of the Bragg angle θ_B and consequently a displacement of the fringes equal to $(L / \cos\theta_B)\Delta\theta_B$. This displacement must again be much smaller than the fringe spacing, *i.e.*

$$(L_0 / \cos\theta_B)(\Delta\lambda / \lambda) \tan\theta_B \ll \lambda L_0 / (t \sin 2\theta_B)$$

or

$$\lambda^2 / \Delta\lambda \gg 2t \sin\theta_B \tan\theta_B. \tag{4}$$

This can be interpreted, in analogy with (3), by saying that the longitudinal (or temporal) coherence length $\lambda^2 / \Delta\lambda$ (Born & Wolf, 1983) must be larger than the projection $(2t \tan\theta_B)$ of the influence domain, along the direction of the incoming beam. It should be underlined that these results can also be obtained using the formalism of the dynamical theory (Mocella *et al.*, 2000).

Conditions (3) and (4) summarize the locally plane wave coherence conditions. Condition (3) is satisfied in our experiments thanks to the long source-to-sample distance on the ID19 beamline of the ESRF.

We have chosen an X-ray energy of 30 keV ($\lambda_0 = 0.37$ Å) and the 111 reflection of a perfect silicon crystal in Laue geometry [$\theta_{B\,(Si\,111)} = 3.78°$].

In order to fulfil the monochromaticity requirement (4), we have selected the 333 reflection of the silicon double monochromator of beamline ID19 at the ESRF for the incident beam.

For the 333 monochromator reflection, the relative bandwidth is $(\Delta\lambda/\lambda_0)_{333} = 7.95 \times 10^{-6}$. We work in the vertical diffraction plane, in which the source size a is minimum ($\sim$50 µm).

3. Application to X-ray refractometry

3.1. Existing refractometric methods

The refractive index n of materials for X-rays is very slightly smaller than unity ($n \sim 1 - 10^{-6}$, $1 - 10^{-7}$) and requires special arrangements to be measured. The interferometric technique, using the Bonse–Hart *L–L–L* interferometer (Bonse & Hart, 1965*a*,*b*, 1968) allows accurate determination of the refractive index (Bonse & Hellkötter, 1969; Bonse & Materlik, 1976; Hart & Siddons, 1981; Templeton *et al.*, 1980) and is generally considered as the most accurate method. The sample to be measured is introduced into one of the interferometer beams and the refractive index is determined by measuring the displacement of the fringes. The sample must be of high quality and the absorption becomes a problem for an energy below 2 keV (Lengeler, 1994).

Another technique is based on the measurement of the critical glancing angle for total external reflection; accurate measurements must take absorption and surface roughness into account (Stanglmeier *et al.*, 1992). Even if such a method is, in principle, less accurate than interferometry, it overcomes some limitations. The measurements can be extended below 50 eV or bulk material can be used, whereas interferometry requires thin materials because of absorption.

The measurement of the refractive index using the angular deviation through a prism is the oldest method, also for X-rays. The experimental set-up, however, is different from the classical one of visible optics, because the refractive index is very close to unity. In the X-ray set-up (James, 1965), a small beam is refracted, near glancing-incidence condition, at the first surface of the prism of apex angle 90° and exits perpendicularly through the other surface without refraction. The deviation of the beam is measured, using the subharmonic beam ($\lambda/2$) which is totally reflected on the first surface. This

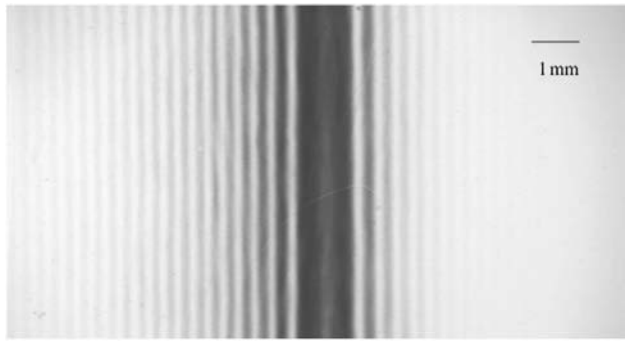

Figure 2
Example of a locally plane wave topograph. Silicon 111 reflection for an energy of 30 keV.

technique has been revisited by Fontaine *et al.* (1985) to measure the refractive index of GaAs near the Ga and As *K* edges, using synchrotron radiation. Their measurements present a strong discrepancy with the theory near the As edge: this could not be completely corrected by taking into account absorption (Warburton & Ludwig, 1986).

Another type of experimental set-up for measurement of a refractive index with a prism has been used by Malgrange *et al.* (1968). It is based on the angular amplification produced in a perfect crystal under the condition of Bragg diffraction.

The angular deviation induced by a prism can also be measured with a monolithic Laue–Laue diffractometer (Deutch & Hart, 1984*a*,*b*) which allows angle measurements with an accuracy of 60 µs.

3.2. The present method

The locally plane wave set-up produces an oscillatory profile $I(x) = R(x/L_0 \cos\theta_B)$ (Fig. 2) which can be used as the reference to analyse the phase modification induced when introducing an object in a part of the incident beam, along the path between the source and the crystal analyser. The general relation between the phase modulation $\varphi(x)$ and the local angular deviation $\varepsilon(x)$ is

$$\varepsilon(x) = (\lambda/2\pi)(\mathrm{d}\Phi/\mathrm{d}x). \tag{5}$$

A prism is a simple phase object that introduces a constant linear gradient in the phase of the incident wave.

The angular deviation of the beam, of apex angle 2α (Fig. 3), through the prism is

$$\varepsilon = \delta\,[\tan(\varphi) + \tan(2\alpha - \varphi)], \tag{6}$$

where the real part of the refractive index is $n = 1 - \delta$ and where it is taken into account that $\delta \ll 1$; φ is the angle of incidence on the first surface of the prism. The prism creates a virtual image S' of the source S. S' is clearly separated from S, because the distance $\overline{SS'}$ is the product of the angular deviation ε by the very large source-to-crystal distance L_0. The point at the exact Bragg position, on the entrance surface, is displaced by $\Sigma = \overline{SS'} = \varepsilon L_0$. Thus the Σ displacement of the fringe pattern is also

$$\Sigma = \varepsilon L_0 = \delta\,[\tan(\varphi) + \tan(2\alpha - \varphi)]L_0. \tag{7}$$

By inserting the prism into a part of the incident beam only, we obtain both the displaced and the non-displaced patterns on the same image. The displacement Σ, from which we can calculate δ, is thus easily measured. This measurement may be easily repeated for different wavelengths by changing the monochromator setting.

The accuracy of δ depends on the accuracy of the measurement of the displacement Σ (this is limited by the detector resolution, which is the grain size of the film in the present case). Therefore it is suitable to increase the displacement Σ by increasing the bracketed term in (7). This can be achieved by working under grazing-incidence conditions. This implies, however, that the path of the beam inside the sample becomes larger. If the photoelectric absorption of the material is large, the contrast in the image may become too weak.

On the other hand, the accuracy of the measurement depends also on the accuracy of the determination of both angles α and φ. The relative error is minimum if these angles are approximately equal. In such a case, the displacement Σ [equation (7)] is then not too sensitive to the value of φ,

$$\Sigma = \varepsilon L_0 = 2\delta L_0 \tan\alpha. \tag{8}$$

In order to demonstrate the validity of our technique, we have performed measurements with a prism of aluminium and with a prism of plexiglas; the apex angle 2α of both prisms was 90° and the incidence angle $\varphi = \alpha = 45°$.

Fig. 4 presents the fringes displacement induced by the plexiglas prism for an energy of 30 keV. In a direction perpendicular to the fringes, the displacement is $\Sigma = 85$ µm from which we calculate the real part of the refractive index decrement $1 - n = \delta = 2.9 \times 10^{-7}$, which is correct. For aluminium we have obtained $\delta = 6.0 \times 10^{-7}$, which is also good.

This technique using a fixed crystal analyser could be extended to the case of more complicated phase objects,

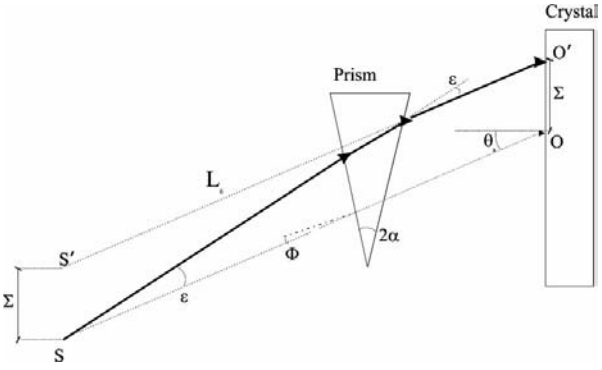

Figure 3
Schematic representation of the set-up: a prism is placed in the incident beam. One measures the displacement Σ in the fringe pattern to measure the angular deviation due to the refraction in the prism.

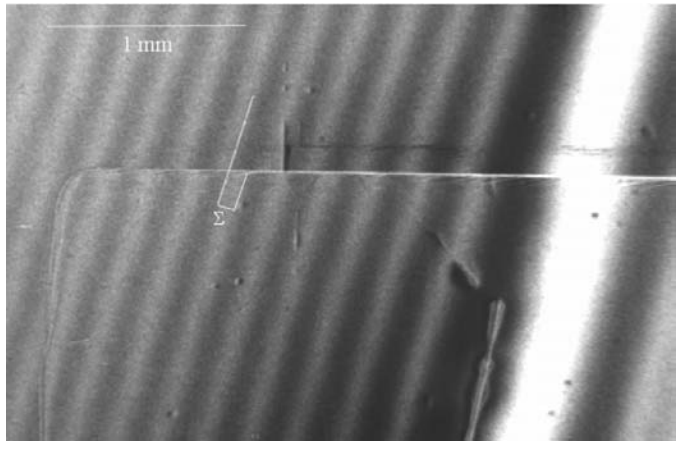

Figure 4
Superposition of the fringe diffraction patterns. The pattern with the plexiglas prism is located in the lower part of the figure. The displacement Σ, measured in a direction perpendicular to the fringes, is clearly visible.

similarly to the differential phase-imaging technique using a rotating crystal analyser, as shown by Forster *et al.* (1980), Davis *et al.* (1995*a*,*b*), Bushuev *et al.* (1996), Nikulin (1997) and Chapman *et al.* (1998). Such techniques are notably different from the phase contrast method based on free-space propagation, without crystal analyser (Cloetens *et al.*, 1996).

4. Visualization of the strain field around an isolated defect.

X-ray diffraction topography is used to visualize defects in crystalline materials. However, the details of an image are quite difficult to understand because the contrast of the image results from interferences between the wavefields which are diffracted and/or curved in the vicinity of the defect.

A locally plane wave image contains information about the phase of the propagating wave and is thus sensitive to perturbations in the path of the waves inside the crystal. In the previous section, we have exploited this information to measure the angular deviation induced by an object located outside the crystal. We can also consider such deviation induced inside the crystal. The displacement field $u(\mathbf{r})$ associated with a crystal defect leads to an effective local disorientation $\delta\theta$ of the reflecting planes, representing a local variation of the Bragg condition, that can be expressed as (Authier, 1967)

$$\delta\theta(\mathbf{r}) = -\frac{1}{k \sin 2\theta_B}\frac{\partial\{\mathbf{h}\cdot\mathbf{u}(\mathbf{r})\}}{\partial s_h}, \qquad (9)$$

where $\mathbf{h}$ is the reciprocal-lattice vector for the considered reflection and s_h is the coordinate along the diffracted direction.

We thus observe an angular deviation that is the addition of the two contributions (1) and (9),

$$\Delta\theta_{\rm obs}(x) = \Delta\theta_{\rm in}(x) + \delta\theta(x). \qquad (10)$$

$\Delta\theta_{\rm obs}$ can be easily measured using, as reference, the fringe pattern in a part of the crystal far from the defect where the crystal can be considered as perfect.

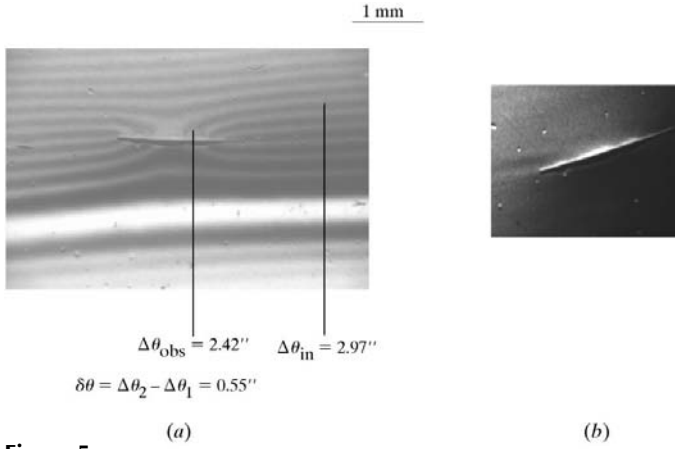

Figure 5
Contour fringes around a scratch. The angular departure is measured by following the fringes from a perfect part of the crystal.

Fig. 5 shows an image of a scratch on the surface of the crystal, for two different settings. Fig. 5(*a*) is the locally plane wave image, Fig. 5(*b*) is a classical topograph using the 111 diffracted wave of the monochromator. The shape of the scratch and a black and white contrast near the core of the defect is the only information contained in Fig. 5(*b*).

In Fig. 5(*a*), one observes the distortion of the perfect pattern fringes induced by the strain field in a large area, quite far from the core of the defect. The fringe pattern represents contour lines for $\Delta\theta_{\rm obs}$. Their value may be known, following all fringes in a perfect area of the crystal, where $\Delta\theta_{\rm obs} = \Delta\theta_{\rm in}$. In a perfect part of the crystal, $\Delta\theta_{\rm in}$ can be found for each fringe by measuring its distance from the fringe corresponding to the exact Bragg condition.

This illustrates a simple procedure to measure the effective misorientation $\delta\theta(x)$, linked to the displacement field $\mathbf{u}(\mathbf{r})$.

When the crystal is slightly rotated, the position of the fringe, corresponding to the exact Bragg incidence along the entrance surface (point *O* in Fig. 1), is shifted. The new fringe pattern crosses the defect differently (Fig. 6); this can be useful

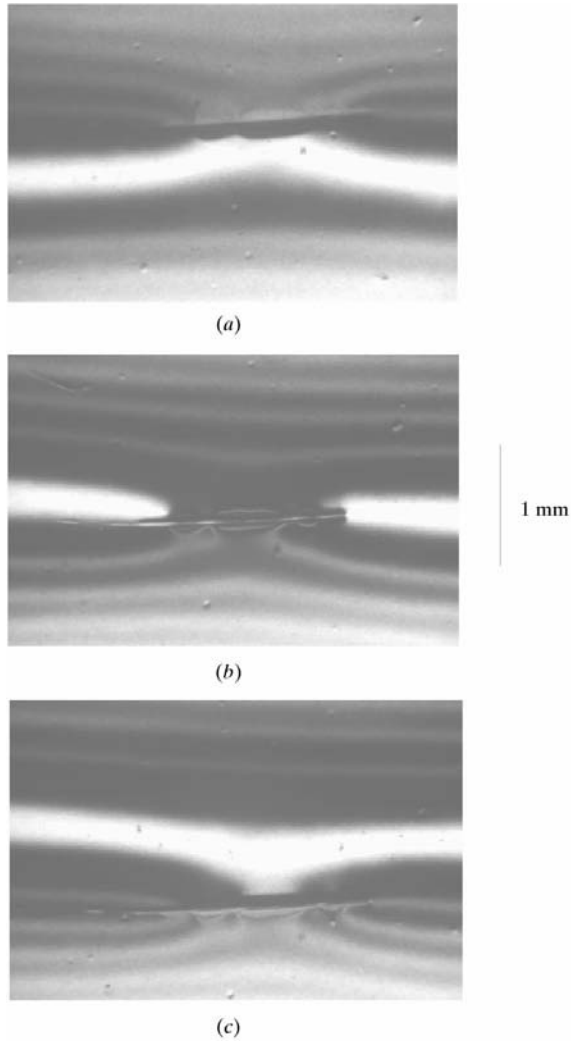

Figure 6
Changes in the contrast of the core of the defect for a larger Bragg angle (*a*), almost at exact Bragg position (*b*) and for a smaller Bragg angle (*c*).

in the analysis of the strain associated with the defect. It can be noted that the black part of the image of the core of the defect is always in the direction of the exact Bragg position (Figs. 6*a* and 6*c*), as expected (Authier, 1967).

By translating the crystal in the beam and/or changing the crystal orientation, one can easily explore the whole volume of the crystal.

5. Conclusions

We have shown that diffraction by a nearly perfect crystal, using a locally incident plane wave, can be used in a number of applications.

The fringe diffraction pattern contains information about the phase of the diffracted wave, which can be used for X-ray refractometry as well as for the visualization of the strain field associated with isolated defects. An advantage of this technique is its simplicity. The experimental set-up used at ID19 of the ESRF is very simple and the interpretation of experimental results is straightforward. The refractive-index measurement, using grazing incidence, can be very accurate and comparable with that of interferometry ($\sim 10^{-3}$). Concerning the strain-field visualization, our technique is comparable in sensitivity with the measurement of minute lattice imperfections using the ultra-plane-wave technique (Kimura *et al.*, 1994; Kawado, 1999), but using a simpler set-up. Analogously to the measurement of spatial coherence in the ultra-plane-wave case (Ishikawa, 1988; Tamasaku & Ishikawa, 2001), the locally plane wave technique can be used for a quantitative measurement of spatial coherence with a simpler experimental arrangement, using a wedge-shaped crystal (Mocella, 1999).

Convergent-beam electron diffraction (CBED) (see *e.g.* Spence & Zuo, 1992), used in electron diffraction, could suggest interesting applications for X-rays with a locally plane wave setting. CBED is equivalent to a rocking-curve method except that, instead of measuring the diffracted intensity as a function of the angle of rotation of the crystal, the incident beam contains a wide range of incident angles. The different diffracted beams contribute to the profile of broadened diffraction spots (Cowley, 1981).

This does not mean that the locally plane wave technique has the same range of applications as CBED. In electron diffraction, multiple-beam scattering is quite usual and the coherent overlapping of CBED patterns for two reflections allows an interferometric imaging (Spence & Cowley, 1978; Tsuda & Tanaka, 1996). This could be investigated for X-rays, using a three-beam diffraction, but might be difficult to realise.

References

Authier, A. (1967). *Adv. X-ray Anal.* **10**, 9–31.
Authier, A. & Simon, D. (1968). *Acta Cryst.* A**24**, 517–526.
Bonse, U. & Hart, M. (1965*a*). *Appl. Phys. Lett.* **6**, 155–156.
Bonse, U. & Hart, M. (1965*b*). *Z. Phys.* **188**, 154–164.
Bonse, U. & Hart, M. (1968). *Acta Cryst.* A**24**, 240–245.
Bonse, U. & Hellkötter, H. (1969). *Z. Phys.* **223**, 345–352.
Bonse, U. & Materlik, G. (1976). *Z. Phys.* B**24**, 189–191.
Born, M. & Wolf, E. (1983). *Principle of Optics*, 6th ed. Oxford: Pergamon Press.
Bushuev, V. A., Ingal, V. N. & Belyaevkaya, A. (1996). *Cryst. Rep.* **41**, 766–774.
Chapman, D., Thomlinson, W., Zhong, Z., Johnston, R. E., Pisano, E., Washburn, D., Sayers, D. & Segre, C. (1998). *Synchrotron Rad. News*, **11**, 4–11.
Cloetens, P., Barrett, R., Baruchel, J., Guigay, J. P. & Schlenker, M. (1996). *J. Phys. D*, **29**, 133–146.
Cowley, J. M. (1981). *Diffraction Physics.* Amsterdam: North Holland.
Davis, T. J., Gureyev, T. E., Gao, D., Stevenson, A. W. & Wilkins, S. W. (1995*a*). *Phys. Rev. Lett.* **74**, 3173–3176.
Davis, T. J., Gureyev, T. E., Gao, D., Stevenson A. W. & Wilkins, S. W. (1995*b*). *Nature (London)*, **373**, 595–598.
Deutch, M. & Hart, M. (1984*a*). *Phys. Rev. B*, **30**, 640–642.
Deutch, M. & Hart, M. (1984*b*). *Phys. Rev. B*, **30**, 643–646.
Fontaine, A., Warburton, W. K. & Ludwig, K. F. (1985). *Phys. Rev. B*, **31**, 3599–3605.
Forster, E., Goetz, K. & Zaumseil, P. (1980). *Krist. Tech.* **15**, 937–945.
Hart, M. & Siddons, P. (1981). *Proc. R. Soc. London*, **376**, 465–481.
Ishikawa, T. (1988). *Acta Cryst.* A**44**, 496–499.
James, R. W. (1965). *The Optical Principles of the Diffraction of X-rays.* Cornell University Press.
Kawado, S. (1999). *Jpn. J. Appl. Phys.* **38**, 520–525.
Kimura, S., Ishikawa, T. & Matsui, J. (1994). *Philos. Mag. A*, **69**, 1179–1187.
Lengeler, B. (1994). *Resonant Anomalous Scattering*, pp. 35–60. Amsterdam: Elsevier.
Malgrange, C., Velu, E. & Authier, A. (1968). *J. Appl. Cryst.* **1**, 181–184.
Mocella, V. (1999). PhD thesis, Université J. Fourier, Grenoble, France.
Mocella, V., Epelboin, Y. & Guigay, J. P. (2000). *Acta Cryst.* A**56**, 308–316.
Mocella, V., Guigay, J. P., Epelboin, Y., Härtwig, J., Baruchel, J. & Mazuelas, A. (1999). *J. Phys. D*, **32**, A88–A91.
Nikulin, A. Yu. (1997). *Appl. Phys. Lett.* **70**, 1545–1547.
Pinsker, Z. (1978). *Dynamical Scattering of X-rays in Crystals*. Berlin: Springer.
Spence, J. C. H. & Cowley, J. M. (1978). *Optik*, **58**, 129–142.
Spence, J. C. H. & Zuo, J. M. (1992). *Electron Microdiffraction.* New York: Plenum Press.
Stanglmeier, F., Lengeler, B., Weber, W., Göbel, H. & Schuster, M. (1992). *Acta Cryst.* A**48**, 626–639.
Tamasaku, K. & Ishikawa, T. (2001). *Acta Cryst.* A**57**, 197–200.
Templeton, D. H., Templeton, L. K., Phillips, J. C. & Hodgson, K. O. (1980). *Acta Cryst.* A**36**, 436–442.
Tsuda, K. & Tanaka, M. (1996). *J. Electron Microsc.* **45**, 59–63.
Warburton, W. K. & Ludwig, K. F. (1986). *Phys. Rev. B*, **33**, 8424–8432.